Assessment of ATV Dynamics Models Used for GNC Design and Validation with Flight Data

Eric Piquemal and Guillaume Pionnier**
*with the support of Olivier Mongrard** and Finn Ankersen***
**Airbus Defence and Space SAS, Les Mureaux, France*
***ESA-ESTEC, Noordwijk, Netherlands*

Abstract

During ATV4 and ATV5 end of mission, high-rate angular velocity measurements were collected. This additional telemetry offers the opportunity to precisely characterize the attitude dynamics of the vehicle. First, the temporal evolution of the angular rate is matched up to GNC commands to estimate the propulsion performance. Then, a spectral analysis is performed to identify the flexible motion. These results are confronted to the parameters of the mathematical models used for the design and validation of ATV GNC algorithms. The paper concludes with a discussion on the representativeness of the models and on the lessons learned for future programmes.

1. Introduction

The Automated Transfer Vehicle (ATV) is the most complex space vehicle ever developed by Europe and most certainly one of the biggest successes of the last decade for Airbus Defence and Space and ESA. Since its maiden flight in 2008, ATV performed five consecutive successful missions to the International Space Station (ISS), thus demonstrating that Europe truly master the Rendezvous technology. After one last controlled destructive re-entry on February 15th 2015, the ATV programme came to an end, leaving as heritage several years' worth of telemetry, some of which still waiting to be explored. With the experience and data gathered from the five ATV missions, it is now time to look back on the development of this ambitious project and draw lessons for the conception of future innovative vehicle.

Figure 1: ATV5 approaching the ISS (Photo: ESA/Roscosmos)

The robust design of the Guidance, Navigation and Control (GNC) algorithms undoubtedly was a key element for the ATV to achieve five perfect docking in a row. The development of these on-board algorithms relied on mathematical models, like the propulsion model or the vehicle flexible dynamics model. These models were used all through the ATV development: from controller synthesis to frequency analysis, from non-real-time GNC design simulators to

Functional Engineering Simulator (FES) and qualification platforms. The representativeness of such models and the associated uncertainties are critical to ensure the desired GNC performance during the realisation of the actual mission. It is even more so during the final part of the Rendezvous, when accuracy and safety constraints are the highest. It is then, when ATV forced translation causes numerous thruster activations, that the controller is the most constrained by propellant sloshing, flexible modes and thrust uncertainties.

The ATV repeated successes undeniably proves that the assumptions for the design of Flight Control algorithms were valid. This good behaviour is confirmed by the extensive GNC post-flight analyses performed for all ATV on the most critical phases (Launch and Early Orbit Phase, Rendezvous and Undocking). For these analyses, the GNC software is run again using interpolated flight telemetry as input data, thus giving access to a wide range of internal variables. This powerful tool is very helpful for failure investigation. Yet, this recurrent post-flight analysis does not provide sufficient material to challenge the dynamics models used for the validation of the ATV flight-software. The study presented in this paper aims at making up for that, focusing on a flight phase where the content of telemetry is more favourable.

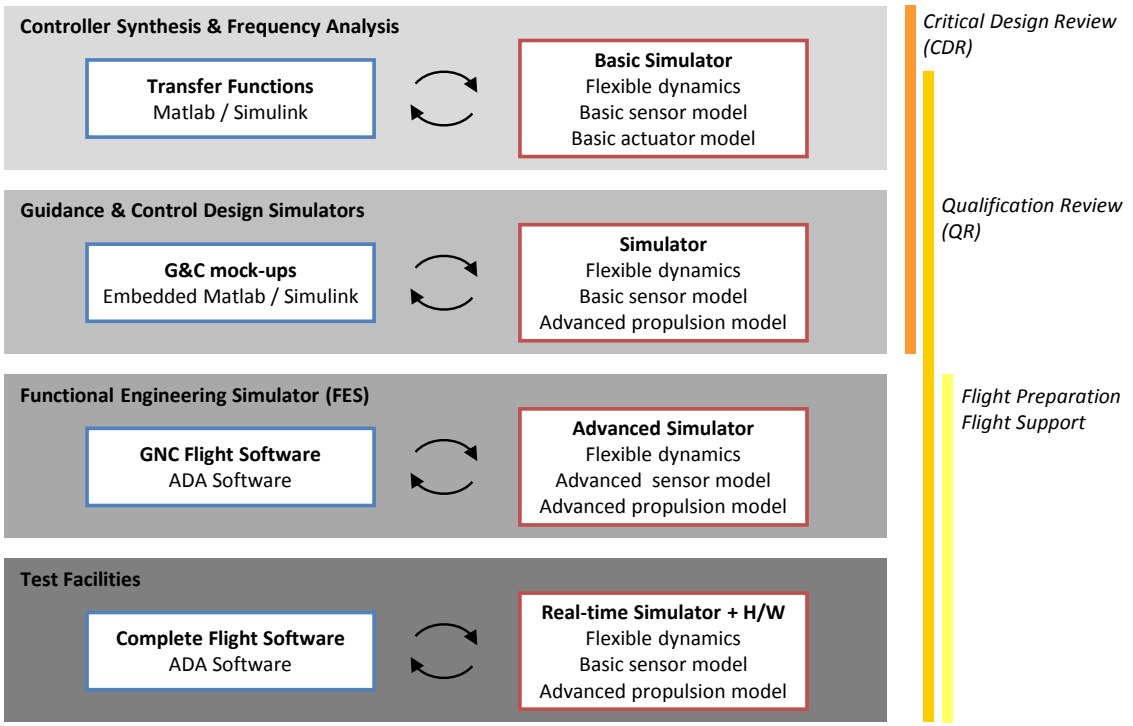

Figure 2: Schematic view of GNC development and validation means

During ATV4 end of mission, investigations on a potential gyrometer failure offered a first opportunity to acquire angular velocity measurements at high rate. Realizing that this telemetry allowed to finely characterize the attitude dynamics of the vehicle, the operation was repeated on ATV5. Based on these navigation measurements, a precise assessment of the effect of propulsion on the dynamics of the vehicle can be made. The high sampling rate of this telemetry also reveals the first solar array bending modes, which are usually concealed in the low-precision low-frequency housekeeping telemetry. The modes frequencies, damping factors and excitabilities become all measurable.

This paper presents a method to estimate the dynamics of the vehicle combining high rate raw gyrometer data with output of the on-board attitude navigation filter. First, the temporal angular rate evolution is matched up to GNC commanded firing duration to estimate the magnitude and direction of the delivered propulsive impulse per thruster. The outcome of this study is compared to the results of the recurring propulsion post-flight analyses, which uses other estimation methods relying on the rich instrumentation of the ATV propulsion system. A second analysis in the frequency domain focuses on retrieving flexible mode definition. The characteristics of the flexible mode are observed at different points in time with different solar array orientations. They are confronted to the parameters of the mathematical models used for the design and validation of ATV GNC algorithms. After comparing the measured

flight dynamics with the models, this paper concludes with a discussion on the representativeness of the models and on the lessons learned for future programmes.

2. Reconstruction of high-rate navigation estimates

2.1 Principles of ATV attitude navigation

The ATV rotational state is estimated on-board by the Absolute Attitude and Drift Estimation (AADE) navigation algorithm running at 1 Hz. This algorithm computes the estimated ATV rotation rate from the gyrometers measurements (angular velocity increments from up to 8 gyrometer axes, at 10 Hz) corrected by an estimated gyro drift. The attitude quaternion is propagated based on the estimated rotation rate. Depending on the availability and reliability of the star-tracker attitude quaternion (1 Hz), the attitude and angular rate are updated with the use of stationary Kalman filters which also provide an estimation of the gyro drift.

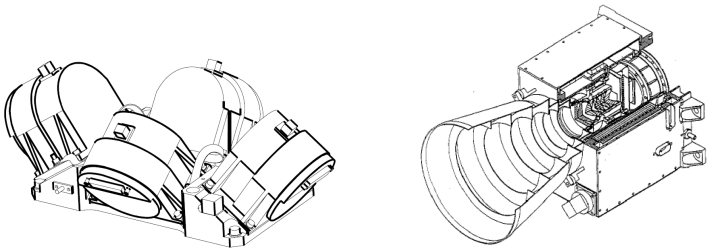

Figure 3: ATV gyrometers and star-tracker used for attitude navigation

The ATV housekeeping telemetry contains sensor data with the same precision as the on-board algorithms: the gyrometer increments at 0.5 Hz and star-tracker measurements at 0.1 Hz. Because of limited bandwidth, the flight software telemetry is truncated with respect to the floating point numbers used on-board. To give orders of magnitude, the Least Significant Bit (LSB) of the navigation angular rate telemetry is about 10^{-5} rad/s when the LSB of gyrometer increments is equivalent to 10^{-6} rad/s. The telemetry sampling rate is also limited: navigation states are at 0.5 Hz for attitude and rate and at 0.1 Hz for gyro drift. If the regular ATV telemetry is enough for the standard monitoring of the vehicle, it is far from the best estimation the sensors can provide.

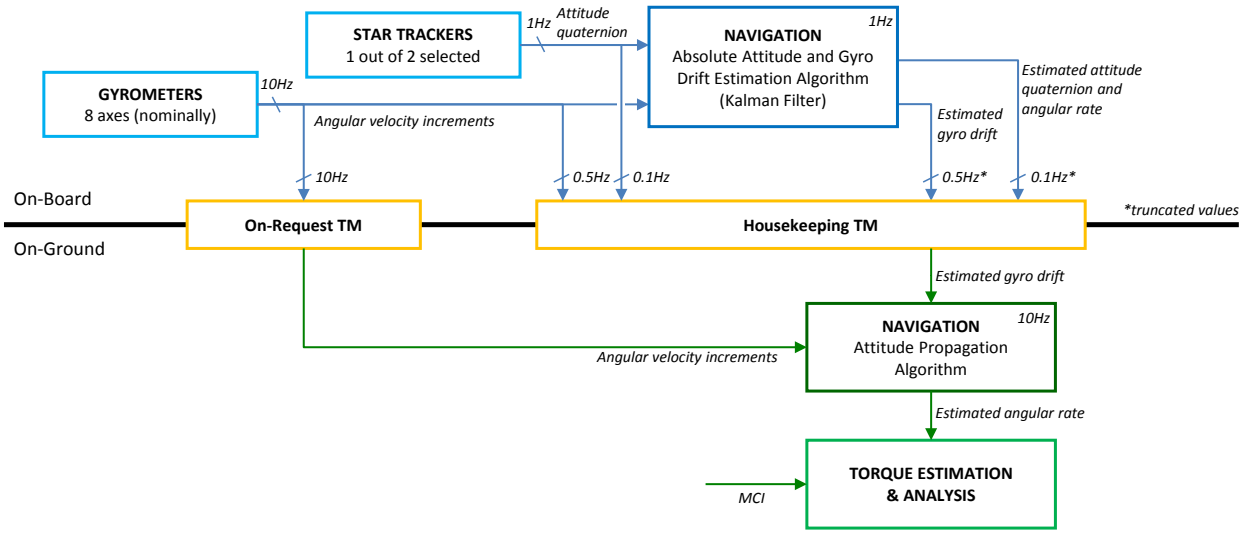

Figure 4: Principles of on-board and on-ground attitude navigation

2.2 Usage of high rate gyrometer telemetry

During ATV4 and ATV5 missions, in the loitering phase between undocking and re-entry, gyrometer increments were momentarily added to the on-request telemetry at 10 Hz. There are four samples about half an orbit each for ATV4 and one sample of one orbit and a half for ATV5, an orbit being roughly 90 minutes on ATV. On ATV4, all four gyrometers were operational at this stage. On ATV5, due to the loss of one power chain, only three gyrometers (six axes) were active.

For this analysis, the angular rate is computed with an exact replica of the on-board algorithm in absence of star-tracker measurement. The gyrometer measurements are derived and corrected by the estimated gyro drift just as they are on-board. The hybridization of star-tracker and gyrometer data is not repeated: the gyro drift estimation is directly imported from the telemetry of the flight navigation filter. It makes sense to do so since the on-board filter processes more sensor data than available in telemetry and the LSB of the downloaded gyro drift is small, about 10^{-7} rad/s, compared to the gyrometer LSB. Figure 5 shows an example of angular rate estimation derived from gyrometer increments with the aforementioned method and compares it to the angular rate provided by navigation in telemetry. The benefit of a smaller LSB and a higher sampling rate is striking: a completely new high-frequency dynamics is revealed.

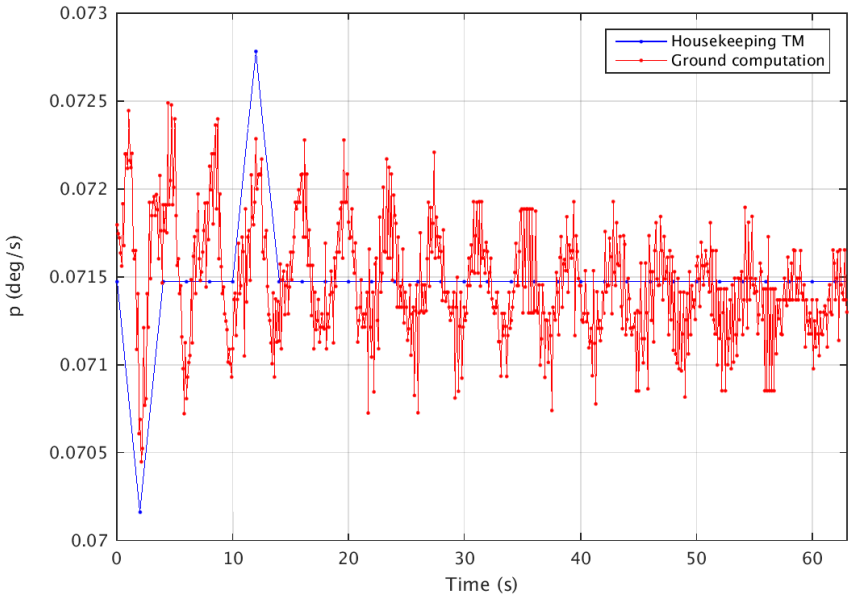

Figure 5: Comparison of the angular rate ground estimation with navigation telemetry

In the end, the additional information provided by the on-request telemetry combined with the housekeeping telemetry gives access to the ATV angular dynamics with at least one more order of magnitude at 20 times the usual frequency.

2.3 Computation of the equivalent external torque

When studying the dynamics of a vehicle, it is more interesting to look at the torques rather than the angular velocities. Therefore, the angular velocity is converted into an equivalent external perturbation torque. It uses for that an estimation of the inertia of the vehicle. The variation of the inertia being negligible with respect to angular accelerations, the equation of the rigid dynamics can be written as follows:

$$T_{ext} = I_{ATV} \times \frac{d\Omega_{ATV/J2000}^{ATV}}{dt} + \Omega_{ATV/J2000}^{ATV} \wedge \left(I_{ATV} \times \Omega_{ATV/J2000}^{ATV} \right) \quad \textbf{(1)}$$

where:

I_{ATV}	is the matrix of inertia in vehicle axes
$\Omega_{ATV/J2000}^{ATV}$	is the angular rate of the vehicle with respect to the inertia frame projected in vehicle axes
T_{ext}	is the equivalent external torque computed at the centre of mass, in vehicle axes

Note that given the angular velocities of ATV (no more than 0.2 deg/s in coasting phases), the gyroscopic torque is very small compared to the angular accelerations in this equation.

An integrated version of this equation is used to estimate the torque impulse generated between two successive angular rate samples, at dates t_n and t_{n+1} separated by Δt. Let there be Ω_n the angular rate at t_n and $\Delta\Omega$ the variation of the angular rate between t_n and t_{n+1}. Assuming a linear variation of the angular rate between the two samples (an assumption is necessary to integrate the gyroscopic term), the torque impulse is expressed as follows:

$$\int_{t_n}^{t_{n+1}} T_{ext} \cdot dt = I_{ATV} \times \Delta\Omega + \Delta t \cdot \left[\left(\Omega_n \wedge I_{ATV} \times \Omega_n\right) + \frac{1}{2}\left(\Omega_n \wedge I_{ATV} \times \Delta\Omega + \Delta\Omega \wedge I_{ATV} \times \Omega_n\right) + \frac{1}{3}\left(\Delta\Omega \wedge I_{ATV} \times \Delta\Omega\right) \right] \quad \textbf{(2)}$$

This equation will be used twice in this study. First, it is used with filtered angular rate measurements to look at the vehicle rigid dynamics and evaluate the propulsion model. These are the results presented in section 3. Second, it is used with raw angular rate measurements, in between thruster activations, to look at the vehicle flexible motion and characterize the solar arrays flexible modes. These are the results presented in section 4.

3. ATV Rigid dynamics

3.1 Vehicle response to propulsion on raw measurements

The torque impulse is first evaluated on the raw angular velocity estimation that was built in section 2.2. The whole on-request telemetry sample is used. As expected and as depicted on Figure 6, the thruster activations stand out in the measured torque impulse.

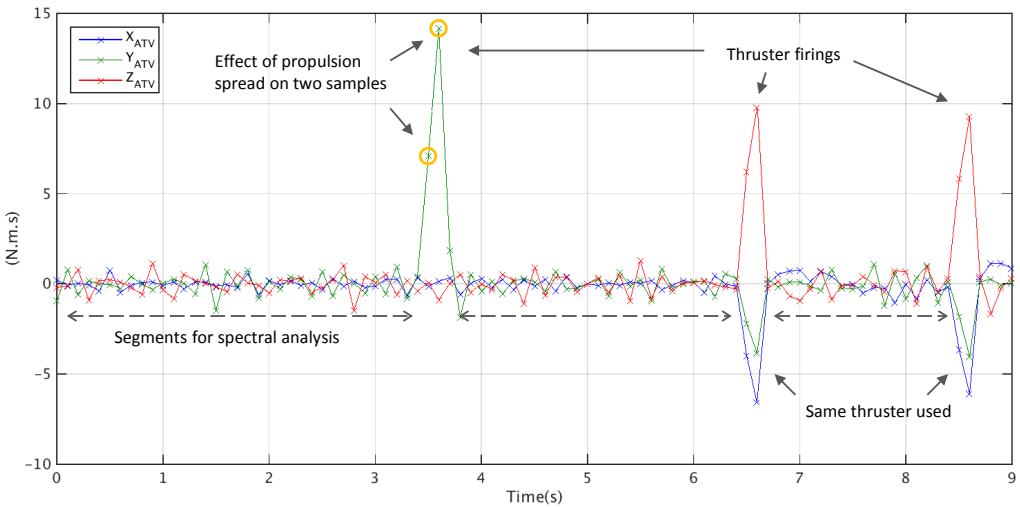

Figure 6 – Torque impulse showing thruster activations

This figure reveals that the propulsion torque impulse is spread over two gyrometer 100 ms samples. This is not consistent with the ATV simulators used for GNC design and validation. On these simulators; the effect of propulsion is visible on a single sample. The reason why the propulsion is seen differently on real gyrometers is unclear and would require further investigations. Still, a few hypotheses can be formulated at this stage. The real shape of the propulsion pulse can differ from the simulators theoretical exponential rise and decay profiles. The scheduling of gyrometer measurements and thruster firings can be such that there is one gyrometer sample right in the middle of a burn. The gyrometer transfer function can spread the pulse over several samples more than expected. Knowing that gyrometers endure extensive tests on ground, a combination of the first two options is the most probable.

3.2 Vehicle response to propulsion on filtered measurements

The torque impulse is now evaluated on the filtered angular velocity to focus on the rigid dynamics and evaluate the propulsion performance. The angular rate measurements are affected by sensor noise and the vehicle flexible motion as illustrated on Figure 5. To limit the analysis to the rigid dynamics, the angular rate is roughly filtered with linear regressions between thruster activations. As a result, the step in angular velocity caused by thruster activation is even clearer as shown on Figure 7.

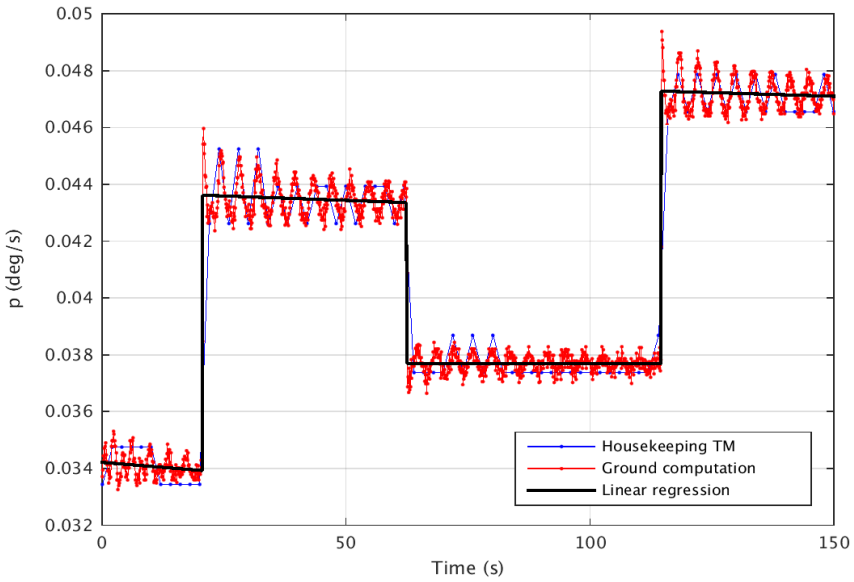

Figure 7: Visualization of thruster activations on filtered and unfiltered angular rate

The equivalent external torque impulse is computed with the filtered angular rate using Equation 2. For each thruster firing, it is compared to the expected torque impulse which is rebuilt based on the on-board propulsion model. This model uses the commanded thruster opening duration, the pressure in propellant lines and the efficiency matrix. Despite the rough approximations that were made, there is a good match between expected and measured impulses. The difference between the observed torque impulse magnitude and the commanded one is plotted Figure 8.

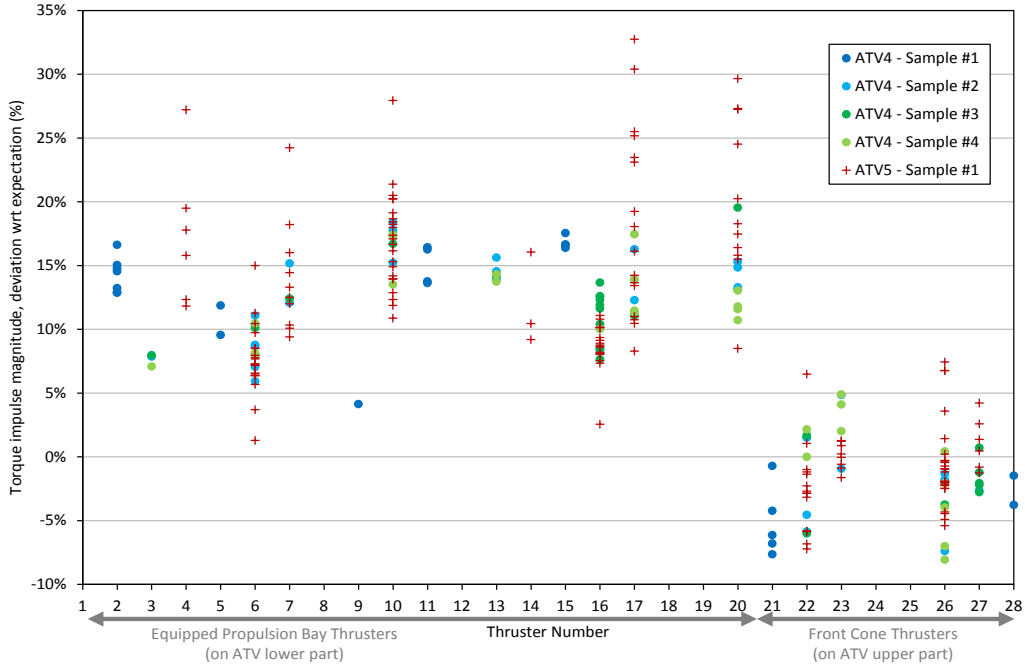

Figure 8: Deviation of the thrust impulse magnitude with respect to the expectation

There are two ways to explain a systematic deviation of the measured impulse with respect to the expected one: individual thruster performances (deviation of thrust magnitude or thrust direction with respect to the on-board model) or Mass Centering and Inertia (MCI) uncertainties.

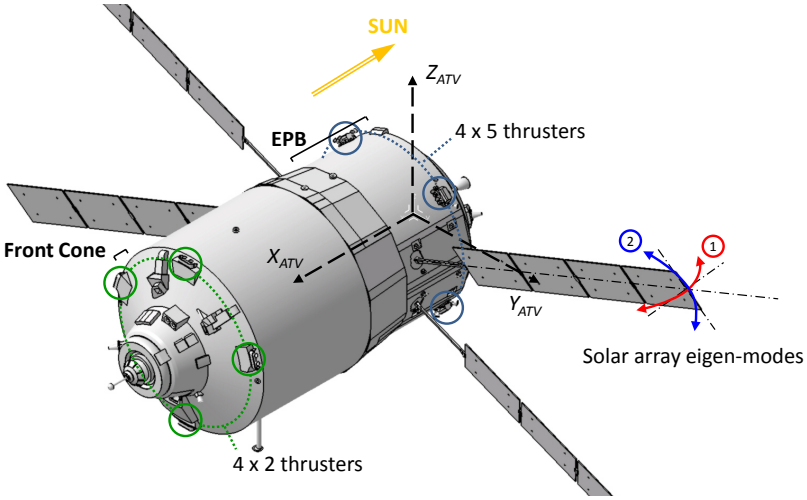

Figure 9: ATV axes and conventions

On Figure 8, it appears clearly that thrusters placed on the Equipped Propulsion Bay (EPB, #1 to #20) produce a higher thrust impulse than expected by GNC whereas thrusters placed on the ATV front cone (#21 to #28) are within expectations. This difference can be explained by pressure losses in front cone thrusters. The pipes feeding the front cone thrusters are several meters longer and have more bends than the pipes feeding the lower thrusters. At Minimum Impulse Bit (MIB) level, it seems like it causes a drop in pressure of about 15 % in front thrusters compared to propulsion bay thrusters. ATV engines are equipped with pressure sensors in the combustion chamber. The recordings of these sensors, shown on Figure 10, confirm this hypothesis and even concur on the magnitude of the pressure drop. The under-performance of front thrusters is also observed on propulsion thermodynamics model but to a lesser extent.

The pressure losses on front cone thrusters are not observed at high activation regimes, this is proven by recurrent propulsion post-flight analysis. Such an asymmetry in the ATV propulsive performance is not taken into account in the ATV controller design. The Thruster Management Function, which converts commanded torques into thruster activations, assumes that all attitude control thruster have the same effectiveness. Knowing that during calm phases the vehicle operates mostly at the MIB, it could have been interesting to fine tune this function based on these observations to enhance the vehicle control.

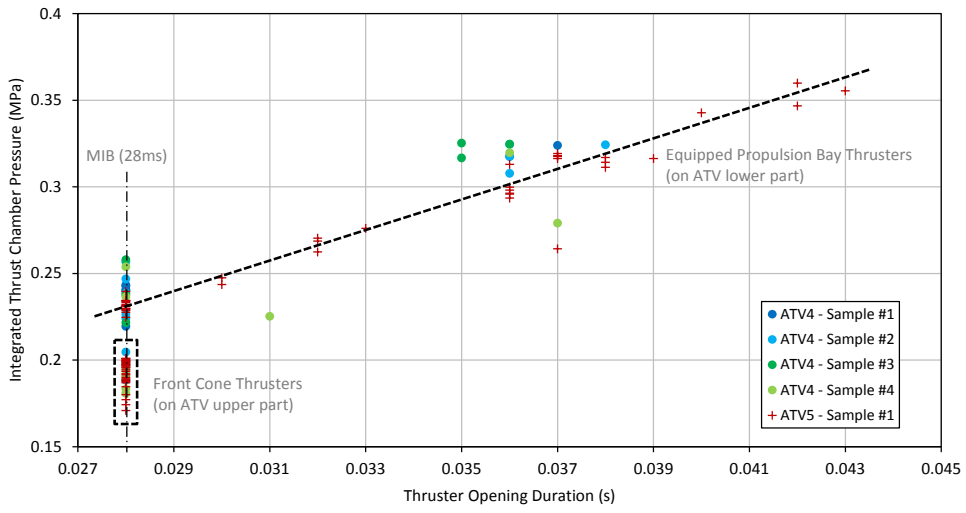

Figure 10: Thruster chamber pressure as a function of opening duration

The nearly 15 % difference between the commanded and the realized torque impulse on Figure 8 shall be confronted to the ATV boost accuracy (directly linked to the force impulse). The analyses of ATV maneuvers using accelerometers and GPS-based orbit determination show that the order of magnitude in boost inaccuracy is about 1 or 2 %. The discrepancy between the force impulse and the torque impulse probably comes from an over estimation of the inertias. In this study, the propellant mass is considered rigidly linked to tank centers whereas in reality a non-negligible part of fuel is sloshing and thus not contributing to the instantaneous value of inertia. The significant amount of fuel remaining in ATV4 and ATV5 tanks after the ISS mission (between 2.5 and 3 tons of propellant for a 16 tons vehicle) could explain this phenomenon. Moreover, the fact that the ATV pressurized module was off-loaded and then reloaded by the ISS crew also adds a lot of uncertainties to the MCI estimation. The characterization of sloshing modes based on this data is not straightforward and would require more advanced (but valuable) study. Indeed, the sloshing modes are below the controller cut-off frequency, which makes them critical for the controller design in particular for Rendezvous and Docking when tracking constraints are the most severe.

3. ATV Flexible dynamics

To study the vehicle flexible dynamics, the torque impulse is computed between each sample of angular velocity as instructed by Equation 2. The spectral analysis is performed on the thrust impulse on segments between thruster activations to observe the vehicle flexible motion.

3.1 Spectral analysis

The Power Spectral Density (PSD) is estimated using Welch's method on long time period without thruster activations (more than 100 s). This is to guarantee a good resolution of the spectrogram and an acceptable level of noise. The PSDs of all selected segments is shown Figure 11.

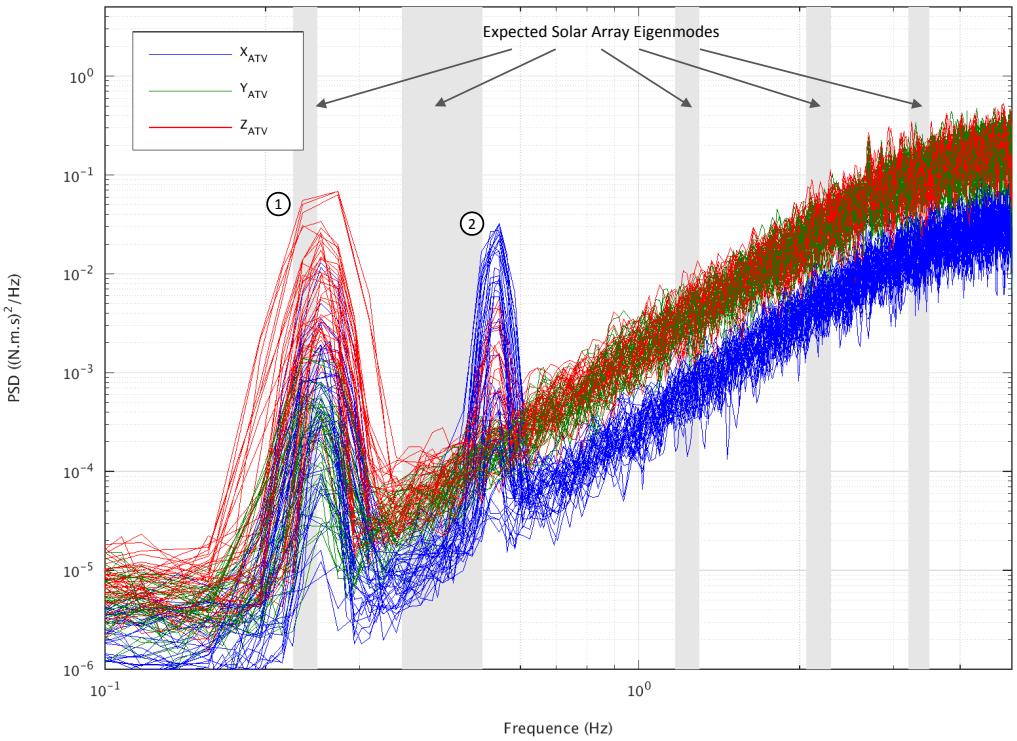

Figure 11: Power Spectral Density of the torque impulse, between two thruster activations, selection of ATV4 data segments

Two frequencies, marked "1" and "2", appear distinctively on the spectrogram. Their components are mostly on the Z axis for the first and on the X axis for the second. These are clearly the two first flexible modes of the solar arrays.

The first mode is the bending of the solar arrays out of their plane; the second mode is the motion of the solar arrays in their plane (flexion of the root hinge). At the time telemetry was collected, the solar panels were oriented with solar cells towards the rear of the vehicle as shown on Figure 9. This geometric configuration explains why the first mode is on Z (yaw axis) and the second one on X (roll axis). It would not have been possible to observe these modes with regular angular rate telemetry. The housekeeping telemetry is at 0.5 Hz, so only modes below the 0.25 Hz frequency would be visible on the Fourier Transform.

The expected frequencies of ATV flexibles modes are shown in grey on Figure 11. Only the first two modes have sufficient effective masses to be visible. The level of excitation of the modes changes with the thruster used and the repetition of propulsion pulses. The observed flexible frequencies are a little higher than expected.

The high frequency noise between 1 Hz and 5 Hz, characterised by its slope on the logarithm plot, is typical of ATV gyrometers.

3.2 Characterization of flexible modes

A key parameter for the control design is the damping of the flexible mode. To evaluate the damping of a mode, the Power Spectral Density is computed with Welch's method as in the previous section, but on sliding windows of 100 s width with 10 s steps.

The results are shown Figure 12 using logarithmic scales. The time dependency is shown by the darkness of the curve: the colour gets lighter and lighter over time, successive curves being separated by 10 s. These figures show that the mode frequency components are stable over time. The damping of the flexible mode is also clearly visible: the attenuation of the second mode is stronger than of the first one. The flexible modes were initially excited by the thruster activation preceding the analysed time frame. The energy monotonically decreases as the mode damps down.

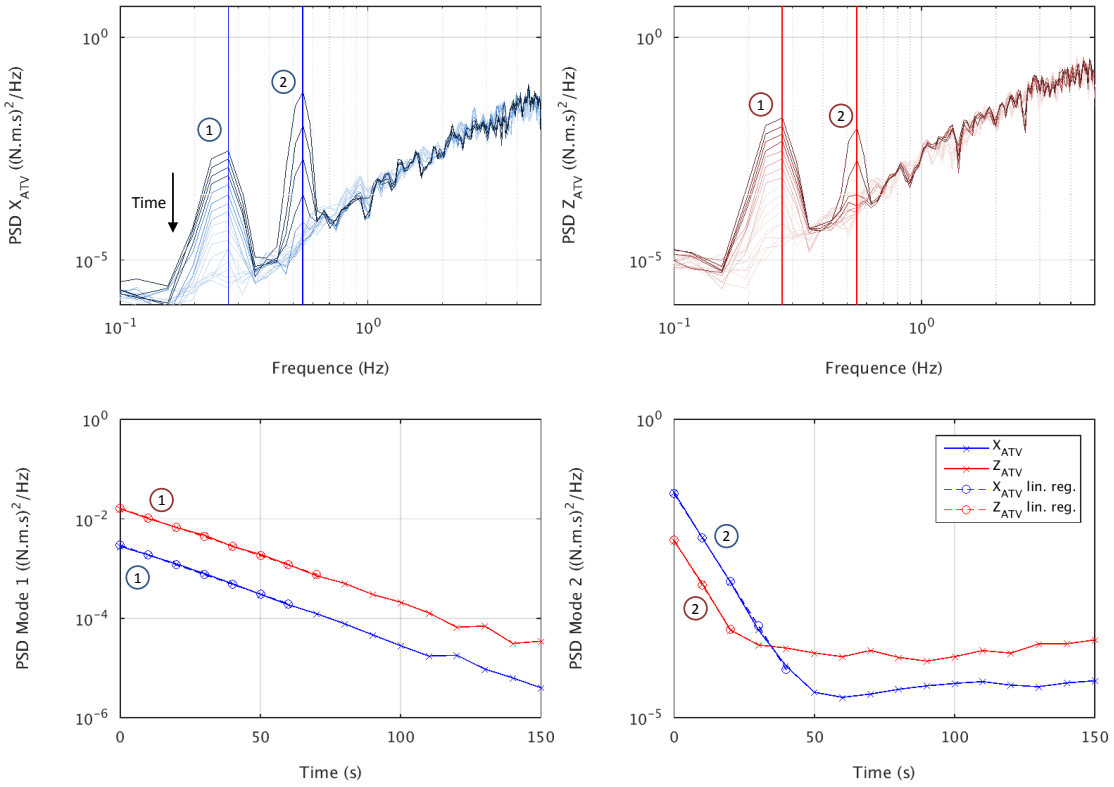

Figure 12 – PSD of torque impulse using sliding windows, visualization of first two mode damping

The magnitude of the PSD at the first two mode frequencies is plotted over time on the bottom plots of Figure 12 (they are like "slices" of Figure 12 top plots). The use of logarithmic scales clearly shows that the attenuation of logarithm of the PSD is linear and so that the decay of the flexible mode amplitude is exponential. This leads to

identify the observed mode with a second order system. The temporal behaviour of a second order system in the canonical form $\ddot{y} + 2\xi\omega_0\dot{y} + {\omega_0}^2 y = 0$ is:

$$y(t) = A \cdot e^{-\xi\omega_0 t} \cdot \cos\left(\omega_0\sqrt{1-\xi^2}\,t + \varphi\right) \quad \textbf{(3)}$$

Where (A, φ) are integration constants. Because the damping is very small compared to 1, when identifying our results with the response of a second order, the pseudo-pulsation $\omega_0 \cdot (1- \zeta)^{1/2}$ is nearly the eigen-pulsation ω_0. The PSD of such a system decreases like $\exp(-2 \cdot \xi \cdot \omega_0 \cdot t)$ at the eigen-frequency. So the damping is worth $-1/(2 \cdot \omega)$ times the variation rate of the PSD logarithm. The variation rate of the PSD is estimated by linear regression as shown on Figure 12 bottom curves. In average the damping of the first mode is 1.4 % and the damping of the second mode 2.4 %. This last figure is smaller than the damping used in ATV GNC validation simulators, 3.4 % on nominal simulations. However, it is not as small as the very conservative 0.5 % took for controller synthesis (notching of flexible modes) and frequency analysis.

3. Conclusion

This paper presents various results. It reveals that it is possible to truly enhance the ATV angular velocity readings using high rate gyrometer telemetry, therefore opening new perspectives of post-flight analysis. This is yet another proof of the value of on-request telemetry. Its capacity to spy all bus traffic (including sensor raw measurement) makes it essential for failure investigation. But, as successfully demonstrated here, it can also be used to increase our technical knowledge of the vehicle, especially for what cannot be fairly tested on ground like dynamics or propulsion.

First focusing on the vehicle rigid dynamics, this study shows that ATV thrusters often deliver more torque than the attitude controller expects. It also points out that, at the MIB activation regime, front cone thrusters are markedly less efficient than propulsion bay thrusters, which was not anticipated. It does not mean the GNC qualification is at stake. In the validation process, uncertainties on thrust and MCI covered these propulsive model errors, thus ensuring the GNC robustness. The study also looks into ATV flexible dynamics. The spectral analysis exposes the first two bending modes of the solar arrays. Even though the characteristics of those modes are slightly off their expected values, they are not as severe as the assumptions taken for controller synthesis.

This article brings forward discrepancies between the mathematical models used for ATV GNC development and flight data. The conservative assumptions in the design made the Flight Control robust enough to ensure perfect operations, as brilliantly demonstrated by the five successful missions to the ISS. Should the ATV programme have gone beyond the fifth unit, it would have been interesting to use this feedback to improve the overall GNC performance. Nonetheless, the ATV flight data can still have a part in the success of upcoming programmes. Pursuing a little further this study, numerical models and associated uncertainty could be revised, hence contributing to the improvement of design and validation of future orbital vehicles.

References

[1] G. Personne, A. Lopez-y-diaz, P. Delpy. 2005. ATV GNC synthesis: overall design, operations and main performances. In: *6th International ESA Conference on Guidance, Navigation & Control Systems, Loutraki, Greece*.

[2] X. Clerc, D. Berthelier, M. Chaize, H. Clerc, E. Meunier, M. Zink, S. Strandmoe. 2008. Qualification of the Automated Transfer Vehicle Flight Control. In: *7th International ESA Conference on Guidance, Navigation & Control Systems, Tralee, Ireland.*

[3] S. Strandmoe, E. DePasquale, I. Escane, M. Augelli, G. Personne, B. Cavrois, N. Fau, M. Yu, M. Zink, X. Clerc, M. Chaize, H. Clerc, E. Gogibus, P. Brun, S. Roussel, H. Requiston, R. Delage, F. Martel, S. Chavy, Ch. Veltz, F. M. Martinez Fadrique, I. Juarez, C. M. Casas-Cuadrado, M. Bonnet, D. Caluwaerts. 2008. Automated Transfer Vehicle (ATV) Flight Control Achievements. In: *7th International ESA Conference on Guidance, Navigation & Control Systems, Tralee, Ireland*.

[4] J. Bourdon, P. Delpy, M. Ganet, I. Quinquis, F. Ankersen. Application of H infinity design on ATV control loop during rendezvous phase. 2002. In: 5*th International ESA Conference on Guidance, Navigation & Control Systems, Frascati, Italy*.